





Fermi-LAT Detected Gamma-ray Emission Likely Associated with SNR Kes 78

YUN-ZHI SHEN(沈蕴之) ¹, YANG CHEN(陳陽) ^{1,2}, XIAO ZHANG(張瀟) ³ AND CHEN HUANG(黃晨) ¹

¹*School of Astronomy & Space Science, Nanjing University, 163 Xianlin Avenue, Nanjing 210023, China*

²*Key Laboratory of Modern Astronomy and Astrophysics, Nanjing University, Ministry of Education, Nanjing 210023, China*

³*School of Physics & Technology, Nanjing Normal University, No.1 Wenyuan Road, Nanjing 210023, China*

ABSTRACT

We have analyzed the GeV gamma-ray emission in the region of the supernova remnant (SNR) Kes 78 using ~16.7 years of *Fermi*-LAT observations and found that the catalog sources 4FGL J1852.4+0037e and 4FGL J1851.8–0007c are better represented as two extended sources modeled as *2Ext*. One of them, designated as E2, is located at R.A.= 282.86°, Dec.= –0.11° with the 68% containment radius $R_{68} = 0.31^\circ$, and is detected with a significance of 15.2σ in the 0.2–500 GeV energy range. The gamma-ray emission of source E2 is well described by a log-parabola (LogP) spectral model with spectral index $\Gamma = 1.2$ and curvature $\beta = 0.3$. The fitting with electron-proton number ratio $K_{ep} = 0.01$ indicates that the GeV emission of source E2 is dominated by hadronic emission. Given the dense molecular environment surrounding the middle-aged SNR Kes 78, the hadronic scenario provides a natural explanation for the observed GeV emission. The extended source E2 can also be replaced with two point sources. One of them, designated as PTS1, is coincident with the newly discovered PSR J1852–0002g within the 68% positional uncertainty circle, indicating a possible gamma-ray contribution from this PSR. The gamma-ray spectrum of source PTS1 can be well described by a LogP spectral shape. The synchro-curvature radiation model provides a satisfactory spectral fit for source PTS1, suggesting that some of the GeV emission from the Kes 78 region might possibly originate from the magnetosphere of PSR J1852–0002g.

Keywords: High Energy astrophysics (739) — Gamma-rays (637) — Supernova remnants (1667) — Pulsars (1306)

1. INTRODUCTION

Supernova remnants (SNRs) are widely regarded as prominent Galactic particle accelerators, capable of accelerating particles to energies of several hundred TeV. Observations from the *Fermi*-LAT have shown that the GeV gamma-ray emission from middle-aged SNRs is typically attributed to hadronic processes, where gamma-rays are produced via the decay of neutral pions created in proton-proton interactions (e.g., W51C, W28, W44; A. A. Abdo et al. 2009a, 2010; Y. Cui et al. 2018; M. Cardillo et al. 2014; G. Peron et al. 2020). Multi-wavelength studies are consistent with or further support this interpretation by revealing spatial correlations between the gamma-ray emission and the adjacent molecular clouds (MCs) associated with the SNRs (e.g., B. Liu et al. 2015; W.-J. Zhong et al. 2023; Y.-Z. Shen et al. 2025; P. K. H. Yeung et al. 2023). In some cases, there are both SNR and pulsar (PSR) in a GeV gamma-ray emission region. The GeV gamma-ray emission from PSRs originates from high-energy processes occurring within their magnetospheres, primarily through synchrotron and curvature radiation mechanisms (P. Meszaros 1992). This study focuses on the gamma-ray emission from the SNR—MC interaction region of SNR Kesteven 78 (G32.8–00.1; hereafter Kes 78), aiming to assess the potential contribution from hadronic processes. Meantime, the recent discovery of PSR J1852–0002g, located to the east of the SNR shock boundary, introduces the possibility of an additional contribution from pulsar-related emission.

SNR Kes 78 exhibits an ellipse-like morphology in both radio and X-ray bands, with its structure appearing elongated along the north—south orientation and compressed in the east—west (J2000). A 1720 MHz OH maser has been detected along the eastern

boundary of Kes 78, at coordinates ($18^{\text{h}}51^{\text{m}}48^{\text{s}}.04$, $-00^{\circ}10'35''$; J2000) and a local standard of rest (LSR) velocity V_{LSR} of $+86.1 \text{ km s}^{-1}$ (B. Koralesky et al. 1998), providing robust evidence for shock interaction between the SNR and surrounding MCs. The SNR has been suggested to be associated with molecular gas at a systemic V_{LSR} of approximately $+81 \text{ km s}^{-1}$ (P. Zhou & Y. Chen 2011). The kinematic distance to the SNR is estimated as 4.8 kpc based on the $V_{\text{LSR}} \sim +81 \text{ km s}^{-1}$ for both CO (P. Zhou & Y. Chen 2011) and HI (S. Ranasinghe & D. A. Leahy 2018) observations, and $\sim 5.4 \text{ kpc}$ for H_2 emission line method with the V_{LSR} of $+90 \text{ km s}^{-1}$ (Y.-H. Lee et al. 2020). We will parameterize the distance of SNR Kes 78 as $d = d_5 \text{ kpc}$. P. Zhou & Y. Chen (2011) has reported the underionized hot ($\sim 1.5 \text{ keV}$), low-density ($\sim 0.1 \text{ cm}^{-3}$) inter-cloud plasma and inferred the age of the remnant as about 6 kyr. X-ray observations with *Suzaku* suggest that Kes 78 is a middle-aged remnant with an estimated age of approximately $2.2 \times 10^4 \text{ yr}$, indicating an average shock velocity of $500 - 700 \text{ km s}^{-1}$ (A. Bamba et al. 2016). *XMM-Newton* observations reveal that the eastern region of Kes 78 contains cooler and denser plasma than that in the western region, which may signal interaction between the SNR shock and adjacent MCs (M. Miceli et al. 2017). To the east of SNR Kes 78, a TeV source HESS J1852–000 was detected (H. E. S. S. Collaboration et al. 2018). PSR J1852–0002g, located to the east of the SNR shock boundary, is identified by FAST (J. L. Han et al. 2021) with a spin period of 0.24510 s at a distance of 5.6 kpc. X. He et al. (2022) investigates the distribution of GeV gamma-ray emission in the region surrounding SNR Kes79 using 11.5 years of *Fermi*-LAT observations, identifying two distinct sources, Src-N and Src-S. Notably, Src-S is located to the southeast of SNR Kes 79 with an angular radius of 0.58° , and encompasses SNR Kes 78. However, as early as the release of the 4FGL-DR2 catalog, based on 10 years of data, a gamma-ray source was already reported to the east of SNR Kes 78’s shock boundary (S. Abdollahi et al. 2020; J. Ballet et al. 2020). These detections motivate a dedicated investigation of the GeV gamma-ray emission potentially associated with SNR Kes 78.

In this work, we resolve the GeV gamma-ray emission associated with SNR Kes 78 and also possibly PSR J1852–0002g and explore the origin of the emission. By analyzing the 16.7 yr *Fermi*-LAT data, we resolve an extended source overlapping Kes 78 and fit the spectral energy distribution (SED) to examine the emission mechanisms. We also employ the synchro-curvature model to study the possible contribution from PSR J1852–0002g. The observational data are described in Section 2 and the analysis results are presented in Section 3. The results are discussed in Section 4.

2. OBSERVATIONS AND DATA

2.1. *Fermi*-LAT Observation Data

For the gamma-ray emission, we use 16.7 yr observation data of Large Area Telescope (LAT) onboard the *Fermi Gamma-ray Space Telescope*. The time frame of our research is from 2008-08-04 15:43:36 (UTC) to 2025-04-02 00:50:50 (UTC), and the circular region of interest (ROI) is 15° in radius, centered at the coordinates R.A.= 282.97° , Dec= -0.12° (J2000). We use the software *Fermipy*⁴ (Version 1.3.1 released on 2024 August 20), which is based on the *Fermitools*⁵ (Version 2.2.0 released on 2022 June 21), to analyze the data. We select ‘SOURCE’ class (evclass=128, evtype=3) with the instrument response function (IRF) ‘P8R3_SOURCE_V3_v1’ and constrain the energy range to 0.2 – 500 GeV. To eliminate the Earth’s limb, we limit the maximum of zenith to 90° . We also apply the recommended filter string ‘(DATA_QUAL>0)&&(LAT_CONFIG==1)’ to choose the good time intervals. We construct the background model by integrating gamma-ray sources from the *Fermi*-LAT Fourth Source Catalog Data Release 4 (4FGL-DR4, incorporating updates from 4FGL-DR3; J. Ballet et al. 2023; S. Abdollahi et al. 2022) with the ROI to study the gamma-ray sources, with the Galactic diffuse emission modeled using *gll_iem_v07.fits* and isotropic emission (*iso_P8R3_SOURCE_V3_v1.txt*). To enable a refined spatial analysis, we exclude the PSF0 data and reselect the ‘CLEAN’ class (evclass=256, evtype=56)⁶ using the IRF ‘P8R3_CLEAN_V3::PSF’⁷. This IRF is associated with the isotropic background model corresponding to each PSF type (e.g., *iso_P8R3_CLEAN_V3_PSF_v1.txt* for PSF1).

2.2. Molecular Line Data

We use the archival data of the ^{12}CO ($J=1-0$) line at 115.271 GHz and the ^{13}CO ($J=1-0$) line at 110.201 GHz of the FOREST Unbiased Galactic plane Imaging survey with the Nobeyama 45 m telescope (FUGIN; T. Umemoto et al. (2017)) observation. The angular resolution was $20''$ for ^{12}CO and $21''$ for ^{13}CO , and the average rms noise was $\sim 1.5 \text{ K}$ for ^{12}CO and $\sim 0.7 \text{ K}$ for ^{13}CO at a velocity resolution of 0.65 km s^{-1} .

⁴ <https://fermipy.readthedocs.io/en/stable/>

⁵ <http://fermi.gsfc.nasa.gov/ssc/data/analysis/software/>

⁶ https://fermi.gsfc.nasa.gov/ssc/data/analysis/documentation/Cicerone/Cicerone_Data/LAT_DP.html

⁷ <https://fermi.gsfc.nasa.gov/ssc/data/access/lat/BackgroundModels.html>

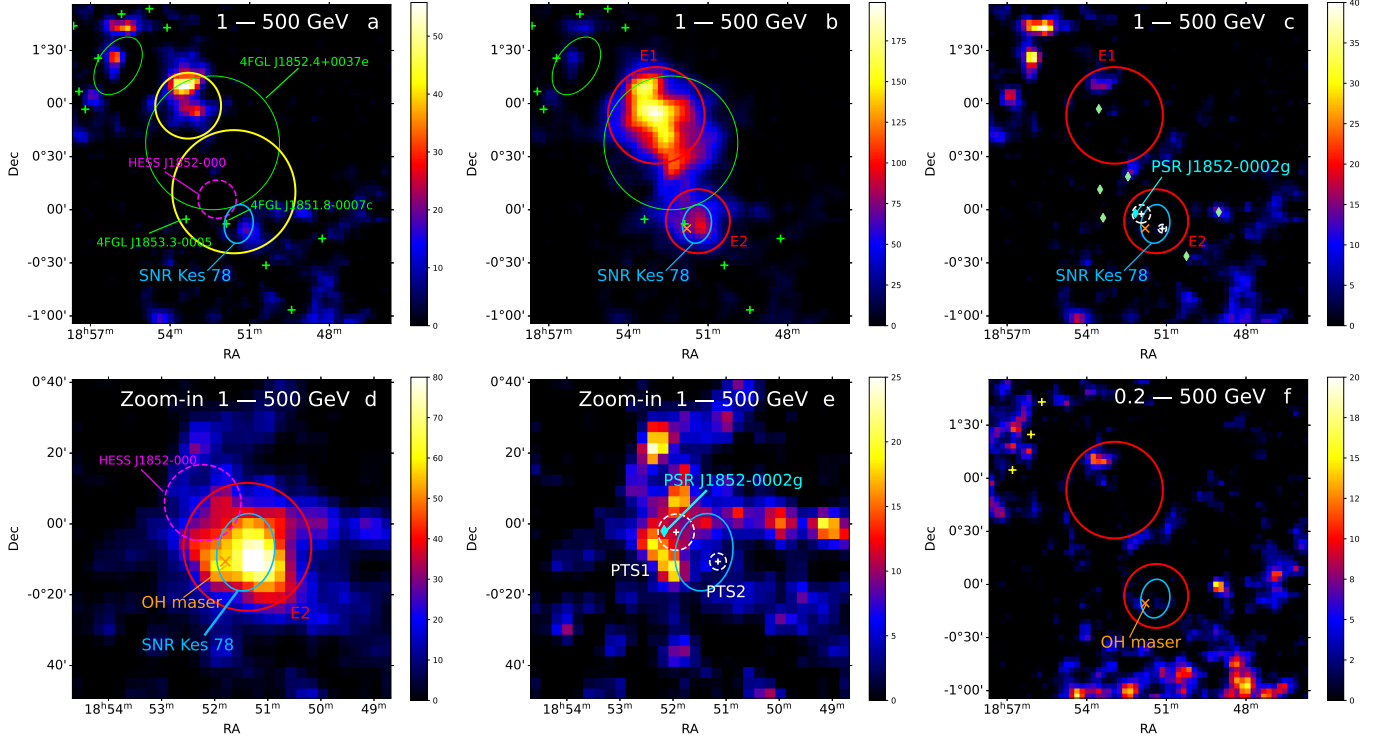


Figure 1. TS maps of $3^\circ \times 3^\circ$ field covering SNR Kes 78 of *Fermi*-LAT in 1 - 500 GeV and 0.2 - 500 GeV. The image scale of the TS maps is 0.05° per pixel. *a*) TS map of 4FGL-DR4 catalog model. *b*) TS map of catalog model without 4FGL J1852.4+0037e and 4FGL J1851.8-0007c in the spatial model. *c*) Residual TS map of spatial model *2Ext* in the energy range of 1 - 500 GeV, with the maximum residual value within source E1 equal to 15.7. *d, e*) Zoomed in TS distribution of sources ‘E2’ and ‘PTS1’ of $1.5^\circ \times 1.5^\circ$ field, respectively. *f*) Residual TS map of spatial model *2Ext* in the energy range of 0.2 - 500 GeV, with the maximum residual value within source E1 equal to 11.8. The yellow circles in panel *a* are the extension of sources Src-N and Src-S in X. He et al. (2022). The green circle and crosses in panels *a* and *b* are the 4FGL-DR4 catalog sources and the two red circles indicate the 68% containment radii of sources in the spatial model *2Ext*. The dashed magenta circles in panels *a* and *d* indicate the TeV source HESS J1852-000. The blue ellipse represents the position of SNR Kes 78, and the orange crosses in panels *c* and *f* mark the position and spatial extent of the 1720 MHz OH maser. The light-green diamonds in panel *c* mark the PSRs with the spin-down energy above 1×10^{34} erg s^{-1} and the cyan diamond marks the PSR J1852-0002g. The dashed white circles and crosses in panels *c* and *e* are the point sources in *1Ext 2PS* model listed in Table 1. The yellow crosses in panel *f* mark the sources added in the background spatial model, which are listed in Table 2.

2.3. Other Data

We use the SARAO MeerKAT 1.3 GHz Galactic Plane Survey (SMGPS) continuum image with an angular resolution of $8''$ (S. Goedhart et al. 2024) to delineate the radio brightness distribution of the SNR.

3. FERMI-LAT GEV GAMMA-RAY EMISSION ANALYSIS

3.1. Spatial Analysis

In the vicinity of SNR Kes 78, two sources, 4FGL J1851.8-0007c and 4FGL J1852.4+0037e, are listed in the 4FGL-DR4 catalog. To reduce statistical uncertainties, we select photon events with energies above 1 GeV and exclude the PSF0⁶ data. In the spatial model fitting, we allow the spectral parameters of the sources within a 5° radius from the center of ROI to vary freely, along with the parameters of the Galactic diffuse and isotropic background components. We then generate residual test statistic (TS) maps centered on the ROI center for both the catalog model and the model in which the two aforementioned sources are removed. The TS is defined as $TS = 2 \log (\mathcal{L}_1 / \mathcal{L}_0)$, where \mathcal{L}_0 and \mathcal{L}_1 represent the maximum likelihood values under the null hypothesis and the alternative hypothesis (with a test source at each pixel), respectively. As shown in Figure 1a, for the catalog model, residual gamma-ray emission remains in the northeastern region of the catalog source 4FGL J1852.4+0037e. In contrast, Figure 1b, the residual map without subtracting the emission of catalog sources 4FGL J1852.4+0037e and 4FGL J1851.8-0007c reveals a distinct gamma-ray emission peak in the northeast in the map and a structure extending southwestward from the peak, which cannot be well modelled by the catalog sources.

Table 1. Best-fitted spatial parameters for all three models.

Model name	Source Name	R.A.(J2000) ^a (°)	Dec.(J2000) ^a (°)	Extension (R_{68}) ^b (°)	Δk	ΔAIC
<i>catalog</i>	4FGL J1852.4+0037e	283.1	0.63	0.63	0	0
(1Ext 1PS)	4FGL J1851.8–0007c	282.97	–0.12	—		
<i>catalog refit</i>	E1	283.24 ± 0.02	0.89 ± 0.02	$0.45^{+0.02}_{-0.03}$	0	–136.7
(1Ext 1PS)	PTS0	282.83 ± 0.02	-0.13 ± 0.03	—		
<i>2Ext</i>	E1	283.24 ± 0.02	0.89 ± 0.02	$0.45^{+0.02}_{-0.03}$	1	–171.2
	E2	282.86 ± 0.03	-0.11 ± 0.03	0.31 ± 0.04		
<i>1Ext 2PS</i>	E1	283.24 ± 0.02	0.89 ± 0.02	$0.45^{+0.02}_{-0.03}$	4	–146.2
	PTS1	282.99 ± 0.09	-0.04 ± 0.05	—		
	PTS2	282.79 ± 0.03	-0.18 ± 0.03	—		
<i>He2022</i>	Src-N	283.33	0.98	0.31	1	–129.6
(X. He et al. 2022)	Src-S	282.90	0.17	0.58		

^a Fitted position coordinates with 1σ uncertainty if available.

^b 68% containment radius with 1σ uncertainty if available.

Table 2. The extra point sources added in the background model.

Source	R.A.(J2000) (°)	Dec.(J2000) (°)
BPS1	284.03	1.41
BPS2	283.92	1.72
BPS3	284.20	1.08

We therefore reanalyze the spatial distribution of GeV gamma-ray emission in this region. Using the `extension` method provided by `Fermipy`, we refit the catalog source 4FGL J1852.4+0037e to determine its best-fit position and spatial extension. Additionally, we apply the `localize` method to refit the spatial parameters of the catalog source 4FGL J1851.8–0007c and the `extension` method to test its spatial extension. The 68% containment radius, R_{68} , is adopted to describe the extension of extended sources. The extension significance is quantified by the test statistic $TS_{\text{ext}} = 2 \log(\mathcal{L}_{\text{ext}}/\mathcal{L}_{\text{PS}})$, where \mathcal{L}_{ext} and \mathcal{L}_{PS} are the maximum likelihoods of the extended and point-source hypotheses, respectively. A source is considered extended if $TS_{\text{ext}} > 16$. We also compare two spatial templates for modeling extended sources: a uniform disk and a radial Gaussian profile. We find the difference of their likelihood values is less than 2, which indicates no significant differences in the fitting results between the two templates, and thus adopt the Gaussian template for subsequent analyses. To further confirm the extended nature of a source, we follow the approach of J. Lande et al. (2012) by comparing an extended source model with a two point-source model. The comparison is quantified using the test statistic $TS_{2\text{PTS}} = 2 \log(\mathcal{L}_{2\text{PTS}}/\mathcal{L}_{\text{PS}})$, where $\mathcal{L}_{2\text{PTS}}$ and \mathcal{L}_{PS} represent the likelihoods of the two point-source model in *1Ext 2PS* and single point-source model in *1Ext 1PS*, respectively.

In the following we use four spatial models to fit the gamma-ray emission of catalog sources 4FGL J1851.8–0007c and 4FGL J1852.4+0037e. In the model names, *Ext* is the notation of extended source, which is chosen as the Gaussian template, and *PS* stands for point source.

1. *catalog* (1Ext 1PS) includes the two catalog sources 4FGL J1851.8–0007c and 4FGL J1852.4+0037e, as the baseline model.
2. *catalog refit* (1Ext 1PS) is the refitted catalog model. The refitted source 4FGL J1852.4+0037e is denoted as ‘E1’ and the refitted source 4FGL J1851.8–0007c as ‘PTS1’.
3. *2Ext* is the model in that the source ‘PTS0’ is replaced with the extended source ‘E2’, the parameters of which are obtained by applying `extension` method to 4FGL J1851.8–0007c.
4. *1Ext 2PS* model includes the extended source ‘E1’ defined in model *2Ext* and two point sources for a comparison with the extended source ‘E2’ defined in the *2Ext* model.

For comparison, we also incorporate the spatial model proposed by X. He et al. (2022), hereafter referred to as *He2022* model.

Table 3. Formulae for gamma-ray spectra

Name	Formula	Free Parameters	Δk	ΔAIC		Γ	$E_{\text{cut/break}}(\text{GeV})$	β
				E2	PTS1			
PL	$dN/dE = N_0 (E/E_0)^{-\Gamma}$	N_0, Γ	0	0	0	—	—	—
ECPL	$dN/dE = N_0 (E/E_0)^{-\Gamma} \exp(-E/E_{\text{cut}})$	$N_0, \Gamma, E_{\text{cut}}$	1	-17.2	-33.0	1.6	1.2	—
LogP	$dN/dE = N_0 (E/E_0)^{-\Gamma-\beta \log(E/E_0)}$	N_0, Γ, β	1	-25.6	-39.0	1.2	—	0.3
BPL	$dN/dE = N_0 \begin{cases} (E/E_b)^{-\Gamma_1} & E \leq E_b \\ (E/E_b)^{-\Gamma_2} & E \geq E_b \end{cases}$	$N_0, E_b, \Gamma_1, \Gamma_2$	2	-20.6	-28.2	1.3 (2.5)	1.0	—

The spatial parameters for all of the models are summarized in Table 1. Each model is implemented into the source list with power-law (PL) spectral shape, and the fitting is performed using Fermipy. To determine the best-fitting spatial model, we adopt the Akaike Information Criterion (AIC; H. Akaike 1974; J. Lande et al. 2012), defined as $\text{AIC} = 2k - 2\log \mathcal{L}$, where k is the number of free parameters and \mathcal{L} is the maximum likelihood value. The calculated differences in ΔAIC for the various models are listed in Table 1. A more negative AIC value indicates a better-fitting model, and a difference of $|\Delta\text{AIC}| > 10$ is considered as strong evidence in favor of the model with the lowest AIC value. Therefore, the *2Ext* model, which yields the lowest AIC value, is considered the most favorable and is adopted for subsequent analysis. For source E2, as a result of *extension* method, we find that it is significantly extended with $\text{TS}_{\text{ext}} = 34.0$. Based on these criteria, we adopt the *2Ext* spatial model for subsequent analyses. The best-fit spatial parameters of source E2 are: R.A. = $282.86^\circ \pm 0.03^\circ$, Dec. = $-0.11^\circ \pm 0.03^\circ$ (J2000), with R_{68} of $0.31^\circ \pm 0.04^\circ$. As shown in Figure 1c, the residual TS map corresponding to the *2Ext* model reveals minimal residual gamma-ray emission in the region, indicating a satisfactory fit. The TS distribution of source E2 is presented in Figure 1d, which shows that the extent of source E2 overlaps SNR Kes 78. Thus, we focus our subsequent analysis on this source. There are also residual emissions to the northeast of source E1 as seen in Figure 1c. Three additional sources with PL spectral models are needed for fitting these remaining residuals in the background. The spatial parameters of the three sources are listed in Table 2. As shown in Figure 1f, the inclusion of these sources effectively removes significant residual gamma-ray emission from the background.

Additionally, the extended source E2 spatially overlapping SNR Kes 78 also can be fitted by using two point sources (namely, *1Ext 2PS* model) with moderately lower significance ($\text{TS}_{2\text{PTS}} = 17.5$). But we note that the fitted position of source PTS1 is coincident with that of PSR J1852–0002g within the 68% uncertainty range, as can be seen in Figure 1e. Considering this, we use the *tempo2* software to search for possible pulsed signals from this PSR, however, no significant detection was obtained. In the following, we will also analyze the property of source PTS1 of the *1Ext 2PS* model.

3.2. Spectral Analysis

To investigate the spectral properties of source E2 across the full energy range of 0.2 – 500 GeV using all event types, we test three alternative spectral models including log-parabola (LogP), exponential cutoff power-law (ECPL), and broken power-law (BPL), in addition to the simple power-law (PL) model. The functional forms of these spectral models are summarized in Table 3. We also use the AIC method to determine the most appropriate spectral model. While keeping the spectral type of source E1 fixed as PL, we vary the spectral type of source E2. Comparison of the four spectral models as listed in Table 3 shows that the LogP model has the lowest AIC value, and thus it is adopted for refitted 4FGL J1851.8–0007c or source E2. With the best-fitting LogP spectral model, the parameters of which are $\Gamma = 1.2$ and $\beta = 0.3$, the obtained flux in 0.2 – 500 GeV is $2.5 \times 10^{-11} \text{ erg cm}^{-2} \text{ s}^{-1}$, and the luminosity is $7.6 \times 10^{34} d_5^2 \text{ erg s}^{-1}$.

We use the SED method of Fermipy to generate the SED of source E2 in the energy range of 0.2 – 500 GeV by applying the maximum likelihood analysis in eight logarithmically spaced energy bins. In the fitting process, we free the normalization parameters of the sources within 3° from the ROI center and the Galactic background parameters. In the energy bins, when the TS value of source E2 is less than 4, we calculate the 95% confidence level upper limit of flux. The obtained SED is in the left panel of Figure 2. For further comparison, we also generate the SED of source PTS1 in the spatial model *1Ext 2PS* in six logarithmically spaced energy bins, and the results are shown in the right panel of Figure 3 with the LogP spectral model for its lowest AIC value. The obtained flux of source PTS1 in 0.2 – 500 GeV is $1.4 \times 10^{-11} \text{ erg cm}^{-2} \text{ s}^{-1}$, which is 56% of that of source E2. Besides the statistic errors, we calculate the systematic uncertainty by fixing the normalization value of Galactic diffuse background at $\pm 6\%$ of the best-fit value (A. A. Abdo et al. 2009b). The maximum deviation between the spectral results obtained with altered background normalizations and those from the nominal fit is taken as the systematic error. We then combine the statistical and systematic uncertainties in quadrature to obtain the final error bars in our spectral analysis.

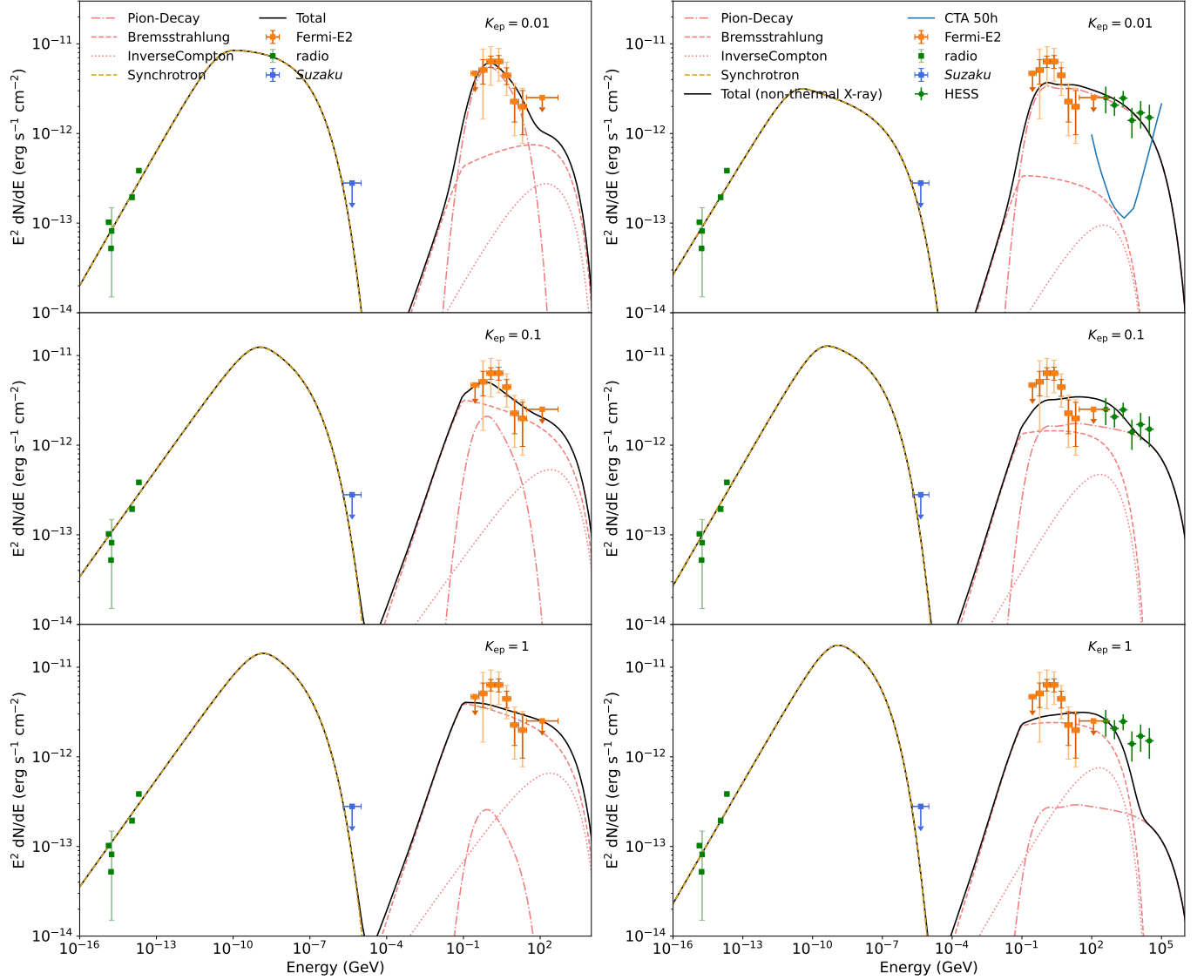


Figure 2. Broadband SEDs of *Fermi*-LAT source E2 with various K_{ep} values. The statistic errors of *Fermi*-LAT data points are in deep colors and the total errors are in light colors. The radio data points of SNR Kes 78 are listed in Table 5, and the X-ray flux is taken from A. Bamba et al. (2016). *Left:* SED fitting for source E2. *Right:* SEDs for both source E2 and HESS J1852-000. The H.E.S.S. data points (green) are adopted from H. E. S. S. Collaboration et al. (2018). The 50 h sensitivity curve of CTA (CTA 2019) is plotted in teal in top right panel.

4. DISCUSSION

Within the spatial range of the gamma-ray source ‘E2’, there are two high energy sources, SNR Kes78 and PSR J1852-0002g, both of which have the ability to emanate GeV gamma rays. Therefore, we here discuss the potential and role of them in the emission by examining the SED of the ‘E2’ (in *2Ext* model) or ‘PTS1’ + ‘PTS2’ (in *1Ext 2PS* model) region

4.1. Emission from SNR Kes 78

As revealed above, the extended GeV source E2, with $R_{68} \approx 0.31^\circ$, projectively covers SNR Kes 78. To analyze the possible origin of the gamma-rays associated with the SNR, we model the gamma-ray spectrum with both hadronic and leptonic mechanisms. We assume that the accelerated particles have a power-law energy distribution with a high-energy cutoff:

$$dN_i/dE = A_i(E_i/1 \text{ GeV})^{-\alpha_i} \exp(-E_i/E_{\text{cut},i}), \quad (1)$$

where $i = e, p$; E_i , α_i , and $E_{\text{cut},i}$ are the particle energy, the power-law index, and the cutoff energy, respectively. The normalization A_i is determined by the total energy above 1 GeV, which is converted from the supernova explosion kinetic energy $E_{\text{SN}} = 10^{51}$

Table 4. SED fitting results.

Components	K_{ep}^a	α	$E_{\text{cut,p}}$ (TeV)	$E_{\text{cut,e}}$ (TeV)	B (μG)	η
source E2	0.01	2.0	0.1	3.6	140	0.004
	0.1	2.2	0.1 ^b	6.6	50	0.004
	1	2.2	0.1 ^b	6.6	45	0.002
E2 & HESS J1852–000	0.01	2.15	1e3	7.4	180	0.007
	0.1	2.1	3e3	5.2	77	0.005
	1	2.1	3e3 ^b	4.9	50	0.002

^a Fixed values in SED fittings.

^b Unconstrained because the hadronic process does not dominate.

erg with a conversion fraction η . We define $K_{\text{ep}} = A_{\text{e}}/A_{\text{p}}$ to control the number ratio of electrons and protons. For electrons, we also take into account the synchrotron cooling effect that the electron index will be steepened by one for the electron energy above $E_{\text{break}} \sim 0.1 \text{ TeV} (B/100 \mu\text{G})^{-2} (t_{\text{age}}/10 \text{ kyr})^{-1}$, where B is the magnetic field strength obtained by SED fittings and t_{age} is the adopted compromised age of SNR Kes 78 as $\sim 10 \text{ kyr}$. We use PYTHON package Naima (V. Zabalza 2015) to calculate the SED considering four radiation mechanisms, synchrotron (F. A. Aharonian et al. 2010), non-thermal bremsstrahlung (A. W. Strong & I. V. Moskalenko 2000), inverse Compton (IC, D. Khangulyan et al. 2014) from the same population of electrons, and pion-decay (E. Kafexhiu et al. 2014) processes. For the IC process, we consider the Galactic disc infra-red background with a temperature of 35 K and an energy density of 0.9 eV cm^{-3} estimated from the interstellar radiation field (T. Shibata et al. 2011) and cosmic microwave background. The detection of the 1720 MHz OH maser on the eastern boundary of the SNR (B. Koralesky et al. 1998), along with studies of the molecular environment (P. Zhou & Y. Chen 2011), has revealed that Kes 78 is interacting with the surrounding MCs. Therefore, molecules can be expected to play an important role in the gamma-ray emission. We adopt $\bar{n}(\text{H}) = 2\bar{n}(\text{H}_2) \sim 70 \text{ cm}^{-3}$ as the average number density of the surrounding target H nuclei for the pion-decay and non-thermal bremsstrahlung processes. The detailed calculation of molecular parameters in the R_{68} region of source E2 is described in Appendix A.

In the SED fitting, we keep the $\alpha_{\text{p}} = \alpha_{\text{e}}$ and the results mainly depend on K_{ep} . For comparison, we incorporate the TeV data points of HESS J1852–000, as reported in H. E. S. S. Collaboration et al. (2018), into the SED fitting. As shown in Figure 2, we separately fit the broadband SEDs for the GeV source E2 alone and for the combined spectrum of E2 and TeV source HESS J1852–000. To constrain the electron cutoff energy $E_{\text{cut,e}}$, we adopt the high-temperature X-ray component reported in A. Bamba et al. (2016), but treated it as purely thermal (because no synchrotron X-rays by the shock front of Kes 78 are detected by XMM-Newton (M. Miceli et al. 2017)), and its flux is adopted as an upper limit for the non-thermal component. The fitting parameters are summarized in Table 4. We see that, as K_{ep} increases, the leptonic processes gradually become dominant; however, both hadronic and leptonic scenarios are capable (or essentially capable) of reproducing the observed data points, except for the TeV range in the leptonic dominant scenario (see bottom right panel in Figure 2). For the Galactic CRs, the value of K_{ep} is typically used as 0.01 (e.g., J. Park et al. 2015; L. Merten et al. 2017). With the adopted $K_{\text{ep}} = 0.01$, the GeV gamma-ray emission is dominated by the hadronic process, with bremsstrahlung providing a subdominant contribution. The magnetic field strength of order $10^2 \mu\text{G}$ is typically seen in the SNRs interacting with MCs, such as CTB 37A (F. Aharonian et al. 2008), W28 (A. A. Abdo et al. 2010), and W44 (Y. Uchiyama et al. 2012), as a result of the compression of gas and magnetic field by the shock interaction.

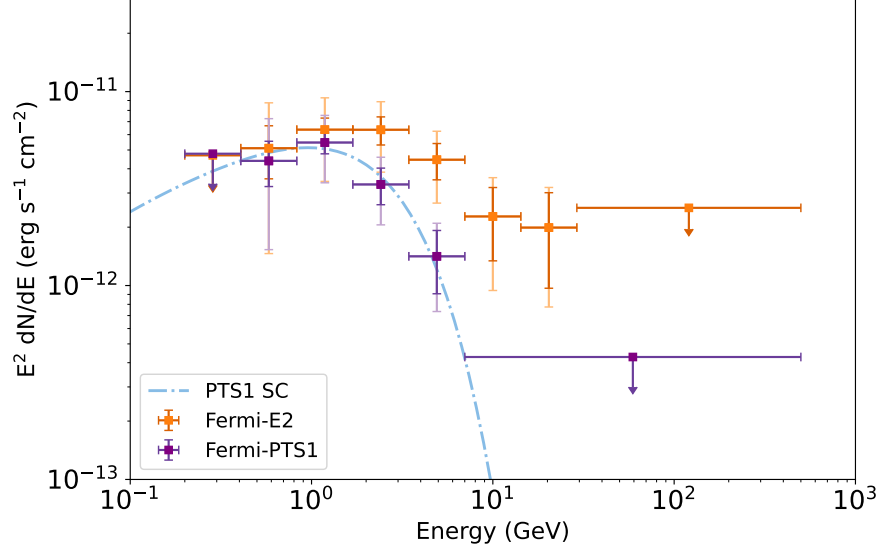
In the right panels of Figure 2, we simultaneously fit the data of the GeV source E2 and HESS J1852–000. As shown in the top and middle right panels (for $K_{\text{ep}} = 0.01$ and 0.1, respectively), the H.E.S.S. data are reproduced by the model and dominated by hadronic process. However, the TeV source does not coincide with the densest MC at $V_{\text{LSR}} = +76 - +88 \text{ km s}^{-1}$ associated with Kes 78; the densest gas is spatially coincident with the GeV source E2 (Figure 4). For the $K_{\text{ep}} = 1$ case, the dominating leptonic processes cannot match the TeV data points with the constrained electron cutoff energy $E_{\text{cut,e}}$. Moreover, as shown in Figure 1d, the R_{68} of source E2 only overlaps a little with the extent of the TeV H.E.S.S. source. Therefore, there may be a possibility that the TeV emission observed by H.E.S.S. may originate from an independent source along the line of sight.

4.2. Synchro-curvature Radiation from PSR J1852–0002g

In Figure 1c, we see that PSR J1852–0002g is inside spatial range (R_{68}) of the extended source E2 and the 68% positional uncertainty circle of the test point source PTS1 in the 1Ext 2PS model. Therefore, a possible gamma-ray contribution from PSR J1852–0002g could not be excluded and is worth estimating. We consider that PSR J1852–0002g emits synchro-curvature (SC) radiation in gamma-rays, appearing as a point source. Thus, we have also analyzed the SED of source PTS1, the flux of which is

Table 5. Details of radio data.

Frequency(GHz)	Flux(Jy)	Reference
0.327	31.3	N. E. Kassim (1992)
0.408	12.8	J. L. Caswell et al. (1975)
0.430	19.0 ± 15.5	J. R. Dickel & L. K. DeNoyer (1975)
2.7	7.2 ± 0.5	T. Velusamy & M. R. Kundu (1974)
5	7.7	J. L. Caswell et al. (1975)

**Figure 3.** SC model for Fermi-LAT source PTS1 with the data points of source E2 for comparison. The format used to represent the errors of the data points is the same as that in Figure 2.

56% of source E2 in 0.2 – 500 GeV (see §3.2 and Figure 3). Note that PTS2 is excluded from the spatial model when the spectrum of source PTS1 is extracted, ensuring that no emission is attributed to PTS2. This provides an estimate of the maximum possible contribution from source PTS1 in this region. We use the same method as that used in A. De Sarkar & P. Majumdar (2024) to treat the SC radiation process and follow the formulae provided by K. S. Cheng & J. L. Zhang (1996); D. Viganò et al. (2015a) to fit the spectrum of source PTS1. The basic formulae of SC radiation used are described in Appendix B.

Similar to D. Viganò & D. F. Torres (2015) and A. De Sarkar & P. Majumdar (2024), we set three free parameters in our calculation: 1) the constant accelerating electronic field $E_{||}$, which is parallel to the magnetic field, determines the energy peak of the spectrum. The range of $E_{||}$ is $\lg(E_{||}/V \text{ m}^{-1}) = 6.5 - 9.5$. 2) The length scale x_0 , which is restricted by the low-energy slope of the spectrum, varies from $x_0/r_c = 0.001 - 1$ (where r_c is the curvature radius). 3) N_0 , the total number of charged particles in the acceleration region, which is in the range of $10^{26} - 10^{32}$ particles.

As in D. Viganò et al. (2015a), the rest parameters are fixed. 1) With the period of PSR J1852–0002g $P = 0.24510$ s (J. L. Han et al. 2021), we assume that r_c is similar to the radius of light cylinder $cP/2\pi \sim 1 \times 10^9$ cm (D. Viganò et al. 2015b). The upper limit of the integral in Eq. B5 and the maximum distance of emitting region is $x_{\max} = r_c = 10^9$ cm. 2) The magnetic field strength B is assumed as $\sim 10^6$ G, which is set to be constant. 3) To numerically solve the momentum equation Eq. B4, the initial values of Lorentz factor and pitch angle are set $\gamma = 10^3$ and $\theta = 45^\circ$, respectively.

We use the SC radiation model to fit the spectra of the point source ‘PTS1’ and the fitting results are: $\lg(E_{||}/V \text{ m}^{-1}) = 7.35$, $x_0/r_c = 0.06$ and $N_0 = 2.3 \times 10^{31}$, with the distance to the PSR adopted as 5.6 kpc (J. L. Han et al. 2021), as shown in Figure 3. Compared with the results of D. Viganò & D. F. Torres (2015), the derived parameters for source PTS1 are generally reasonable. The length scale x_0/r_c is slightly higher than the values reported in their Table 2. The low-energy slope of the source PTS1 spectrum is relatively steep, indicating a preference for a larger x_0 . The SED fitting shows that the emission of the potential point source PTS1 could be explained as SC radiation, indicating that the SC radiation produced by PSR J1852–0002g could take a

part in the detected gamma-rays of source E2. However, the existence of source PTS1 and its potential contribution in this region remain uncertain and require further observational confirmation.

5. CONCLUSION

We have analyzed the GeV gamma-ray emission in the region of the SNR Kes 78 using ~ 16.7 years of *Fermi*-LAT observations. Based on approximately 16.7 years of *Fermi*-LAT data, we find that the catalog sources 4FGL J1852.4+0037e and 4FGL J1851.8–0007c are better represented as two extended sources modeled as *2Ext*. One of them, designated as E1, is the refitted source of the catalog source 4FGL J1852.4+0037e, with the coordinates R.A. = 283.24° , Dec. = 0.89° and $R_{68} = 0.45^\circ$. The other one, designated as E2, is located at R.A. = 282.86° , Dec. = -0.11° with the $R_{68} = 0.31^\circ$, and is detected with a significance of approximately 15.2σ in the 0.2–500 GeV energy range. The emission source E2 is well described by a LogP spectral model with spectral index $\Gamma = 1.2$ and curvature $\beta = 0.3$. The integrated flux in this energy range is 2.5×10^{-11} erg cm $^{-2}$ s $^{-1}$, corresponding to a luminosity of 7.6×10^{34} erg s $^{-1}$, for a distance of 5 kpc. Given the dense molecular environment surrounding SNR Kes 78, together with the typical electron-proton ratio ~ 0.01 , the hadronic scenario provides a natural explanation for the observed GeV emission.

Although the GeV emission in Kes 78 region is best characterized as an extended source E2, it can also be replaced with two point sources. One of them, designated as PTS1, is coincident with PSR J1852–0002g within the 68% positional uncertainty circle, indicating a possible gamma-ray contribution from this pulsar. The gamma-ray spectrum of source PTS1 is well described by a LogP spectral shape. The SC radiation model provides a satisfactory spectral fit for source PTS1, suggesting that some of the GeV emission from the Kes 78 region might possibly originate from the magnetosphere of PSR J1852–0002g. However, no gamma-ray pulsation has been found from the pulsar in our work, possibly due to limited observational sensitivity or inaccurate ephemeris.

LHAASO has detected emission above TeV in the Kes 78 region (i.e., LHAASO J1850–0004u, Z. Cao et al. 2024). The emission properties above TeV are expected to be studied and clarified with LHAASO observation and future CTA observation.

ACKNOWLEDGMENTS

Y.Z.S thanks Wen-Juan Zhong and Jia-Xu Sun for helpful comments. This work is supported by the National Natural Science Foundation of China (NSFC) under grants 12173018, 12121003, and 12393852.

DATA AVAILABILITY

The *Fermi*-LAT data underlying this work are publicly available and can be downloaded from <https://fermi.gsfc.nasa.gov/ssc/data/access/lat/>. We also use the data from FUGIN, FOREST Unbiased Galactic plane Imaging survey with the Nobeyama 45 m telescope, a legacy observation project in the Nobeyama 45 m radio telescope of CO. The MeerKAT 1.3 GHz data used in this work are public in <https://doi.org/10.48479/3wfd-e270> (S. Goedhart et al. 2024).

APPENDIX

A. MOLECULAR PARAMETERS

Following the work of molecular environment of SNR Kes78 by P. Zhou & Y. Chen (2011), we use the FUGIN data to calculate the parameters of the surrounding molecular gas that is likely to be involved in the hadronic interaction responsible for the GeV gamma-ray emission. We extract the averaged CO spectra from the region within $R_{68} \approx 0.31^\circ$ for source ‘E2’ and the region around the OH maser (B. Koralesky et al. 1998), which are marked in Figure 4. According to the Gaussian fitting in the velocity range $\sim +70 - \sim +90$ km s $^{-1}$, we select the local-standard-of-rest velocity V_{LSR} range $+76 - +86$ km s $^{-1}$ to calculate the molecular column density based on the Gaussian fitting results of ^{12}CO and ^{13}CO . We assume that the ^{12}CO lines are optically thick and the ^{13}CO lines are optically thin and calculate the column density for the optically thick and thin cases (J. G. Mangum & Y. L. Shirley 2015, also see therein for detailed definition of the symbols used in the two equations below)

$$N_{\text{thick}} = \frac{3h}{8\pi^3 \mu^2 J_{\mu} R_i} \left(\frac{kT_{\text{ex}}}{hB_0} + \frac{1}{3} \right) \frac{\exp(E_u/kT_{\text{ex}})}{\exp(E_u/kT_{\text{ex}}) - 1} \times \int -\ln \left[1 - \frac{T_{\text{R}}}{J_{\nu}(T_{\text{ex}}) - J_{\nu}(T_{\text{bg}})} \right]^{-1} dv \quad (\text{A1})$$

and

$$N_{\text{thin}} = \frac{3h}{8\pi^3 \mu^2 J_{\mu} R_i} \left(\frac{kT_{\text{ex}}}{hB_0} + \frac{1}{3} \right) \exp \frac{E_u}{kT_{\text{ex}}} \times \left(\exp \frac{h\nu}{kT_{\text{ex}}} - 1 \right)^{-1} \int \tau_{\nu} dv, \quad (\text{A2})$$

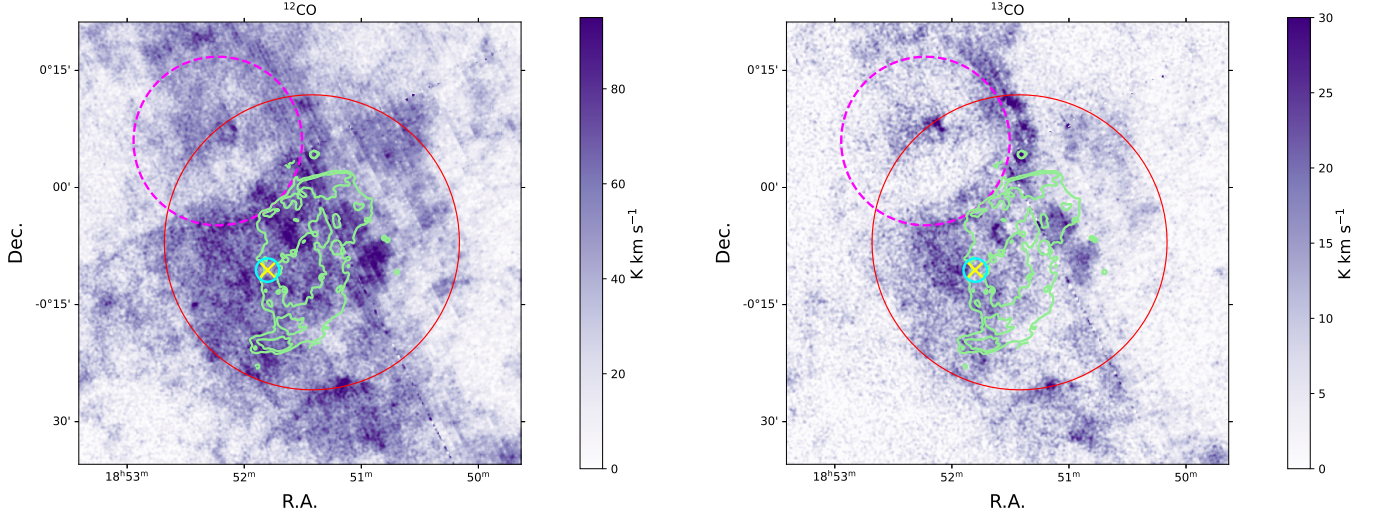


Figure 4. Integrated-intensity greyscale image of ^{12}CO ($J=1-0$) (left panel) and ^{13}CO ($J=1-0$) (right panel) around SNR Kes 78 in the V_{LSR} range $+76 - +88 \text{ km s}^{-1}$ (left panel), overlaid with the SARA MeerkAT Galactic Plane Survey (SMGPS) 1.3 GHz radio continuum contours of the SNR in green. The red circle marks the extended *Fermi*-LAT GeV source ‘E2’ with the radius $R_{68} \approx 0.31^\circ$ around the SNR and the yellow cross is the location of $+86.1 \text{ km s}^{-1}$ OH maser on the SNR’s eastern boundary, surrounded by the cyan circle with the radius of 0.025° ; the two circled (red and cyan) regions are selected for extracting molecular line profiles that are presented in Figure 5. The dashed magenta circles are the position of HESS J1852–000.

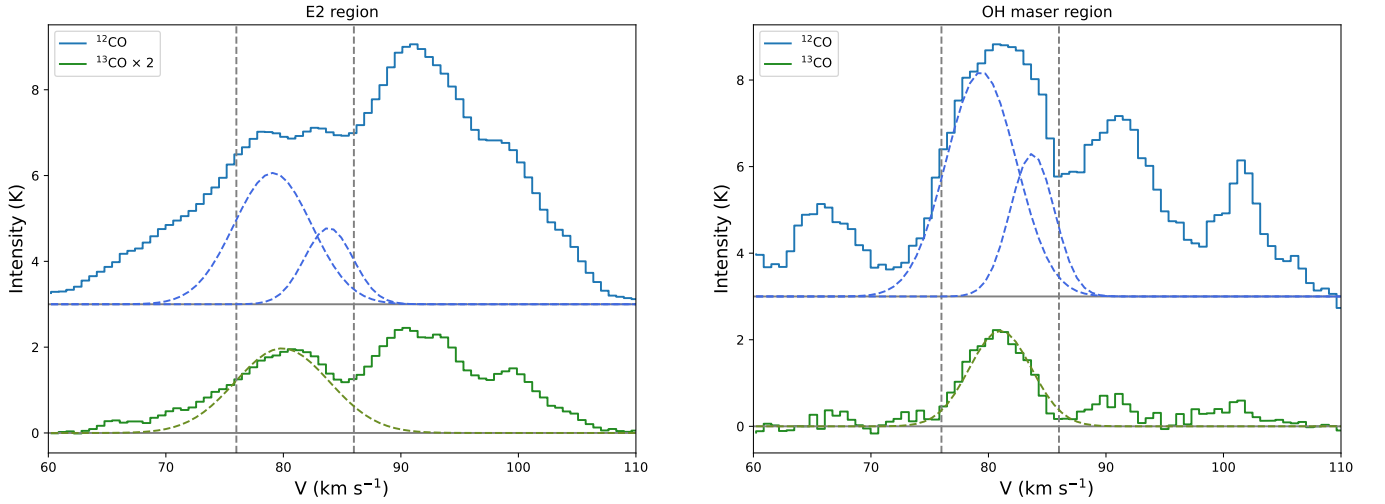


Figure 5. Averaged spectra and multi-Gaussian fitting results in LSR velocity range from $+60 \text{ km s}^{-1}$ to $+110 \text{ km s}^{-1}$ for ^{12}CO and ^{13}CO extracted from ‘E2’ region and OH maser region marked in Figure 4. The gray vertical lines mark the velocity of $+76 \text{ km s}^{-1}$ and $+86 \text{ km s}^{-1}$ (the latter is the velocity of the OH maser).

Table 6. Calculated molecular parameters.

Region	Molecule	$N(\text{species})^a / \text{cm}^{-2}$	$\bar{n}(\text{H}_2) / \text{cm}^{-3}$
E2 R_{68}	^{12}CO	1.2×10^{17}	35
	^{13}CO	8.3×10^{15}	
OH Maser	^{12}CO	2.4×10^{17}	700
	^{13}CO	1.3×10^{16}	

^a Column density of the specific molecular species.

The obtained column densities for the E2 region is $N(^{12}\text{CO}) = 1.2 \times 10^{17} \text{ cm}^{-2}$ and $N(^{13}\text{CO}) = 8.3 \times 10^{15} \text{ cm}^{-2}$.

We calculate the $N(\text{H}_2)$ values with the CO-to- H_2 conversion factor of velocity integrated brightness temperature $N(\text{H}_2)/W(^{12}\text{CO}) \approx 1.8 \times 10^{20} \text{ cm}^{-2} \text{ K}^{-1} \text{ km}^{-1} \text{ s}$ (T. M. Dame et al. 2001). In addition, we also obtain $N(\text{H}_2)$ using abundance ratio $N(\text{H}_2)/N(^{13}\text{CO}) \approx 6 \times 10^5$ (M. A. Frerking et al. 1982). The results obtained by the above two methods are not much different from each other. Assuming that the line-of-sight depth in each region is comparable to the R_{68} for the E2 region and to a radius of 0.025° for the OH maser region, we estimate the mean molecular number density $\bar{n}(\text{H}_2)$. The obtained results are listed in Table 6.

B. SYNCHRO-CURVATURE RADIATION MODEL

The synchro-curvature power radiated by a single particle is given by (see K. S. Cheng & J. L. Zhang 1996; D. Viganò et al. 2015a):

$$\frac{dP_{\text{SC}}}{dE} = \frac{\sqrt{3}e^2\gamma y}{4\pi\hbar r_{\text{eff}}} [(1+z) \int_y^\infty K_{5/3}(y') dy' - (1-z)K_{2/3}(y)], \quad (\text{B3})$$

where K_n are the modified Bessel functions of the second kind of index n , \hbar is the reduced Planck's constant, E is the photon energy, γ is the Lorentz factor of the electron, r_{eff} is the effective radius, and y and z are dimensionless quantities related to photon energy and effective radius, respectively, defined in K. S. Cheng & J. L. Zhang (1996); D. Viganò et al. (2015a).

The evolution of γ and θ (the pitch angle) is obtained by numerically solving the equation for the particle relativistic momentum \mathbf{p} ($=\sqrt{\gamma^2 - 1}mc\hat{\mathbf{p}}$):

$$\frac{d\mathbf{p}}{dt} = eE_{\parallel}\hat{\mathbf{b}} - \frac{P_{\text{SC}}}{v}\hat{\mathbf{p}}, \quad (\text{B4})$$

where E_{\parallel} is the parallel electric field, $\hat{\mathbf{b}}$ is the direction vector of magnetic field, and $\hat{\mathbf{p}}$ is the direction vector of the momentum.

The average SC spectrum throughout the particles' motion trajectory is calculated by the equation

$$\frac{dP_{\text{tot}}}{dE} = \int_0^{x_{\text{max}}} \frac{dP_{\text{SC}}}{dE} \frac{dN}{dx} dx, \quad (\text{B5})$$

where dN/dx is the effective weighted distribution of emitting particles as a function of distance x from the injection point toward the observer. It is given by

$$\frac{dN}{dx} = \frac{N_0 e^{-x/x_{\text{max}}}}{x_0(1 - e^{-x_{\text{max}}/x_0})}, \quad (\text{B6})$$

where $N_0 = \int_0^{x_{\text{max}}} (dN/dx) dx$ is the normalization and x_0 is the length scale of the effective particle distribution.

REFERENCES

- 2019, Science with the Cherenkov Telescope Array (WORLD SCIENTIFIC), doi: [10.1142/10986](https://doi.org/10.1142/10986)
- Abdo, A. A., Ackermann, M., Ajello, M., et al. 2009a, ApJL, 706, L1, doi: [10.1088/0004-637X/706/1/L1](https://doi.org/10.1088/0004-637X/706/1/L1)
- Abdo, A. A., Ackermann, M., Ajello, M., et al. 2009b, ApJL, 706, L1, doi: [10.1088/0004-637X/706/1/L1](https://doi.org/10.1088/0004-637X/706/1/L1)
- Abdo, A. A., Ackermann, M., Ajello, M., et al. 2010, ApJ, 718, 348, doi: [10.1088/0004-637X/718/1/348](https://doi.org/10.1088/0004-637X/718/1/348)
- Abdollahi, S., Acero, F., Ackermann, M., et al. 2020, The Astrophysical Journal Supplement Series, 247, 33, doi: [10.3847/1538-4365/ab6bcb](https://doi.org/10.3847/1538-4365/ab6bcb)
- Abdollahi, S., Acero, F., Baldini, L., et al. 2022, ApJS, 260, 53, doi: [10.3847/1538-4365/ac6751](https://doi.org/10.3847/1538-4365/ac6751)
- Aharonian, F., Akhperjanian, A. G., Barres de Almeida, U., et al. 2008, A&A, 490, 685, doi: [10.1051/0004-6361/200809722](https://doi.org/10.1051/0004-6361/200809722)
- Aharonian, F. A., Kelner, S. R., & Prosekin, A. Y. 2010, PhRvD, 82, 043002, doi: [10.1103/PhysRevD.82.043002](https://doi.org/10.1103/PhysRevD.82.043002)
- Akaike, H. 1974, IEEE Transactions on Automatic Control, 19, 716
- Ballet, J., Bruel, P., Burnett, T. H., Lott, B., & The Fermi-LAT collaboration. 2023, arXiv e-prints, arXiv:2307.12546, doi: [10.48550/arXiv.2307.12546](https://doi.org/10.48550/arXiv.2307.12546)
- Ballet, J., Burnett, T. H., Digel, S. W., & Lott, B. 2020, <https://arxiv.org/abs/2005.11208>
- Bamba, A., Terada, Y., Hewitt, J., et al. 2016, ApJ, 818, 63, doi: [10.3847/0004-637X/818/1/63](https://doi.org/10.3847/0004-637X/818/1/63)
- Cao, Z., Aharonian, F., An, Q., et al. 2024, ApJS, 271, 25, doi: [10.3847/1538-4365/acfd29](https://doi.org/10.3847/1538-4365/acfd29)
- Cardillo, M., Tavani, M., Giuliani, A., et al. 2014, A&A, 565, A74, doi: [10.1051/0004-6361/201322685](https://doi.org/10.1051/0004-6361/201322685)
- Caswell, J. L., Clark, D. H., & Crawford, D. F. 1975, Australian Journal of Physics Astrophysical Supplement, 37, 39
- Cheng, K. S., & Zhang, J. L. 1996, ApJ, 463, 271, doi: [10.1086/177239](https://doi.org/10.1086/177239)

- Cui, Y., Yeung, P. K. H., Tam, P. H. T., & Pühlhofer, G. 2018, *ApJ*, 860, 69, doi: [10.3847/1538-4357/aac37b](https://doi.org/10.3847/1538-4357/aac37b)
- Dame, T. M., Hartmann, D., & Thaddeus, P. 2001, *ApJ*, 547, 792, doi: [10.1086/318388](https://doi.org/10.1086/318388)
- De Sarkar, A., & Majumdar, P. 2024, *A&A*, 681, A34, doi: [10.1051/0004-6361/202347258](https://doi.org/10.1051/0004-6361/202347258)
- Dickel, J. R., & DeNoyer, L. K. 1975, *AJ*, 80, 437, doi: [10.1086/111760](https://doi.org/10.1086/111760)
- Frerking, M. A., Langer, W. D., & Wilson, R. W. 1982, *ApJ*, 262, 590, doi: [10.1086/160451](https://doi.org/10.1086/160451)
- Goedhart, S., Cotton, W. D., Camilo, F., et al. 2024, *MNRAS*, 531, 649, doi: [10.1093/mnras/stae1166](https://doi.org/10.1093/mnras/stae1166)
- H. E. S. S. Collaboration, Abdalla, H., Abramowski, A., et al. 2018, *A&A*, 612, A1, doi: [10.1051/0004-6361/201732098](https://doi.org/10.1051/0004-6361/201732098)
- Han, J. L., Wang, C., Wang, P. F., et al. 2021, *Research in Astronomy and Astrophysics*, 21, 107, doi: [10.1088/1674-4527/21/5/107](https://doi.org/10.1088/1674-4527/21/5/107)
- He, X., Cui, Y., Yeung, P. K. H., et al. 2022, *ApJ*, 928, 89, doi: [10.3847/1538-4357/ac51d6](https://doi.org/10.3847/1538-4357/ac51d6)
- Kafexhiu, E., Aharonian, F., Taylor, A. M., & Vila, G. S. 2014, *PhRvD*, 90, 123014, doi: [10.1103/PhysRevD.90.123014](https://doi.org/10.1103/PhysRevD.90.123014)
- Kassim, N. E. 1992, *AJ*, 103, 943, doi: [10.1086/116116](https://doi.org/10.1086/116116)
- Khangulyan, D., Aharonian, F. A., & Kelner, S. R. 2014, *ApJ*, 783, 100, doi: [10.1088/0004-637X/783/2/100](https://doi.org/10.1088/0004-637X/783/2/100)
- Koralesky, B., Frail, D. A., Goss, W. M., Claussen, M. J., & Green, A. J. 1998, *The Astronomical Journal*, 116, 1323–1331, doi: [10.1086/300508](https://doi.org/10.1086/300508)
- Lande, J., Ackermann, M., Allafort, A., et al. 2012, *ApJ*, 756, 5, doi: [10.1088/0004-637X/756/1/5](https://doi.org/10.1088/0004-637X/756/1/5)
- Lee, Y.-H., Koo, B.-C., & Lee, J.-J. 2020, *AJ*, 160, 263, doi: [10.3847/1538-3881/abc00e](https://doi.org/10.3847/1538-3881/abc00e)
- Liu, B., Chen, Y., Zhang, X., et al. 2015, *ApJ*, 809, 102, doi: [10.1088/0004-637X/809/1/102](https://doi.org/10.1088/0004-637X/809/1/102)
- Mangum, J. G., & Shirley, Y. L. 2015, *PASP*, 127, 266, doi: [10.1086/680323](https://doi.org/10.1086/680323)
- Merten, L., Becker Tjus, J., Eichmann, B., & Dettmar, R.-J. 2017, *Astroparticle Physics*, 90, 75, doi: [10.1016/j.astropartphys.2017.02.007](https://doi.org/10.1016/j.astropartphys.2017.02.007)
- Meszáros, P. 1992, *Journal of the British Astronomical Association*, 102, 287
- Miceli, M., Bamba, A., Orlando, S., et al. 2017, *A&A*, 599, A45, doi: [10.1051/0004-6361/201629842](https://doi.org/10.1051/0004-6361/201629842)
- Park, J., Caprioli, D., & Spitkovsky, A. 2015, *PhRvL*, 114, 085003, doi: [10.1103/PhysRevLett.114.085003](https://doi.org/10.1103/PhysRevLett.114.085003)
- Peron, G., Aharonian, F., Casanova, S., Zanin, R., & Romoli, C. 2020, *The Astrophysical Journal Letters*, 896, L23, doi: [10.3847/2041-8213/ab93d1](https://doi.org/10.3847/2041-8213/ab93d1)
- Ranasinghe, S., & Leahy, D. A. 2018, *The Astronomical Journal*, 155, 204, doi: [10.3847/1538-3881/aab9be](https://doi.org/10.3847/1538-3881/aab9be)
- Shen, Y.-Z., Chen, Y., Zhang, X., et al. 2025, *MNRAS*, 537, 464, doi: [10.1093/mnras/staf008](https://doi.org/10.1093/mnras/staf008)
- Shibata, T., Ishikawa, T., & Sekiguchi, S. 2011, *ApJ*, 727, 38, doi: [10.1088/0004-637X/727/1/38](https://doi.org/10.1088/0004-637X/727/1/38)
- Strong, A. W., & Moskalenko, I. V. 2000, in Book “Topics in Cosmic Ray Astrophysics” (vol.230 in Horizons in World Physics, 81–103, doi: [10.48550/arXiv.astro-ph/9812260](https://doi.org/10.48550/arXiv.astro-ph/9812260)
- Uchiyama, Y., Funk, S., Katagiri, H., et al. 2012, *ApJL*, 749, L35, doi: [10.1088/2041-8205/749/2/L35](https://doi.org/10.1088/2041-8205/749/2/L35)
- Umemoto, T., Minamidani, T., Kuno, N., et al. 2017, *PASJ*, 69, 78, doi: [10.1093/pasj/psx061](https://doi.org/10.1093/pasj/psx061)
- Velusamy, T., & Kundu, M. R. 1974, *A&A*, 32, 375
- Viganò, D., & Torres, D. F. 2015, *MNRAS*, 449, 3755, doi: [10.1093/mnras/stv579](https://doi.org/10.1093/mnras/stv579)
- Viganò, D., Torres, D. F., Hirotani, K., & Pessah, M. E. 2015a, *MNRAS*, 447, 1164, doi: [10.1093/mnras/stu2456](https://doi.org/10.1093/mnras/stu2456)
- Viganò, D., Torres, D. F., Hirotani, K., & Pessah, M. E. 2015b, *MNRAS*, 447, 2631, doi: [10.1093/mnras/stu2564](https://doi.org/10.1093/mnras/stu2564)
- Yeung, P. K. H., Bamba, A., & Sano, H. 2023, *PASJ*, 75, 384, doi: [10.1093/pasj/psad006](https://doi.org/10.1093/pasj/psad006)
- Zabalza, V. 2015, in *International Cosmic Ray Conference*, Vol. 34, 34th International Cosmic Ray Conference (ICRC2015), 922, doi: [10.22323/1.236.0922](https://doi.org/10.22323/1.236.0922)
- Zhong, W.-J., Zhang, X., Chen, Y., & Zhang, Q.-Q. 2023, *MNRAS*, 521, 1931, doi: [10.1093/mnras/stad628](https://doi.org/10.1093/mnras/stad628)
- Zhou, P., & Chen, Y. 2011, *ApJ*, 743, 4, doi: [10.1088/0004-637X/743/1/4](https://doi.org/10.1088/0004-637X/743/1/4)